The Astrophysical Journal, 952:40 (11pp), 2023 July 20 https://doi.org/10.3847/1538-4357/acd44f

Characterizing 3D Magnetic Structures in Sunspot Light Bridges

Ju Jing[1,2], Nian Liu[1,2], Jeongwoo Lee[1,2], Yan Xu[1,2], Wenda Cao[1,2], and Haimin Wang[1,2]
[1] Institute for Space Weather Sciences, New Jersey Institute of Technology, University Heights, Newark, NJ 07102-1982, USA; ju.jing@njit.edu
[2] Big Bear Solar Observatory, New Jersey Institute of Technology, 40386 North Shore Lane, Big Bear City, CA 92314-9672, USA
Received 2022 December 16; revised 2023 May 9; accepted 2023 May 9; published 2023 July 17

Abstract

Light bridges (LBs) are narrow structures dividing sunspot umbra, and their role in active region evolution is yet to be explored. We investigated the magnetic structure of the two LBs: a narrow LB (with width ∼810 km) and a considerably wider LB (2475 km) in the active region NOAA 12371. We employed: (1) the high-spatial-resolution spectropolarimetric data obtained by the Near InfraRed Imaging Spectropolarimeter (NIRIS) of the 1.6 m Goode Solar Telescope (GST) for studying the magnetic structure at the photosphere, and (2) the nonlinear force-free field (NLFFF) models, extrapolated from both the photospheric magnetogram from GST/NIRIS and from the Helioseismic and Magnetic Imager on board the Solar Dynamics Observatory, for studying the three-dimensional (3D) magnetic structure on a larger scale. Our observations reveal the presence of a field-free (or, more precisely, weak-field) region and the different velocity structures inside the two LBs. Analysis of the 3D NLFFF model shows a low-lying magnetic canopy as well as the enhanced current system above the LBs. The substantial difference between the LBs and the umbrae is found in the overall magnetic topology in that the field lines emanating from the two LBs are more twisted than that from the neighboring umbrae.

Unified Astronomy Thesaurus concepts: Sunspots (1653); Solar active region magnetic fields (1975)

1. Introduction

Sunspot light bridges (hereafter referred to as LBs) are intriguing narrow structures dividing sunspot umbrae of the same or opposite magnetic polarity. Physically, LBs are conceived to be intrusions of field-free hot plasma into an otherwise stable umbral magnetic field from below (Parker 1979; Choudhuri 1986; Leka 1997; Spruit & Scharmer 2006), with a magnetoconvective origin (Hirzberger et al. 2002; Rempel et al. 2009; Cheung et al. 2010; Rempel 2011). Based on Parker's hypothetical sketch of the magnetic field over umbral dots (Parker 1979), Leka (1997) proposes a magnetic canopy structure above the LBs, a field-free cusp structure formed by the magnetic field lines on either side of an LB meeting upon the top of the LB and then being forced to converge into a vertical direction. This physical picture is later illustrated in a numerical simulation based on a radiative magnetohydrodynamics (MHD) model (Toriumi et al. 2015a).

For a long time, our knowledge of the magnetic fields of LBs was mainly limited to their basic characteristics, i.e., a weaker magnetic field and more horizontal orientation compared to the nearby umbra (e.g., Beckers & Schröter 1969; Lites et al. 1991; Rueedi et al. 1995; Leka 1997). With the advent of high-resolution solar telescopes, such as the Swedish 1 m Solar Telescope (SST; Scharmer et al. 2003) and the 1.6 m Goode Solar Telescope (GST; Cao et al. 2010; Goode & Cao 2012), we were able to take a closer look at LBs. In high-resolution observations, LBs consist of a chain of convective cells with hot upflows at the center and cold downflows at the edges, similar to the granules in the quiet Sun (e.g., Lagg et al. 2014; Toriumi et al. 2015b; Zhang et al. 2018; Griñón-Marín et al. 2021). Observations also show that LBs are often associated with recurring dynamic phenomena observed in the upper atmosphere, such as chromospheric jets, ejections, and brightenings, which may be the result of small-scale magnetic reconnection in and around the LBs (Shimizu 2011; Bharti 2015; Louis et al. 2015; Toriumi et al. 2015b; Robustini et al. 2016; Yang et al. 2016; Tian et al. 2018; Lim et al. 2020). A strong spatial correlation between electric currents and elevated temperature is found in most regions of the LB spine suggesting that the chromosphere is heated via resistive ohmic dissipation (Louis et al. 2021).

Despite the progress made in understanding the thermodynamic properties of LBs, a direct demonstration of the fine-scale three-dimensional (3D) magnetic structure of LBs remains scarce so far. The weaker and more horizontal photospheric magnetic field of LBs mentioned above provides evidence of a magnetic canopy structure at the visible surface. Jurčák et al. (2006) report for the first time the stratification of magnetic parameters in three atmospheric layers up to 200 km, retrieved from the spectropolarimetric data with the Stokes inversion based on response functions (SIR; Ruiz Cobo & del Toro Iniesta 1992) code. Their results show that the magnetic field strength of LBs is low in the photosphere but increases with height, while inclination with respect to the local vertical decreases with height, coinciding with the expected variation of magnetic canopy structure in the vertical direction. Later, Lagg et al. (2014) performed a spatially coupled inversion to retrieve depth-dependent atmospheric parameters to present a tapered magnetic configuration overarching the upflows on a continuum of optical depth scale. To better represent the 3D magnetic field over LBs, it would be preferable to use a geometric height scale rather than the optical depth scale delivered by inversions. However, the conversion between these two scales is not straightforward due to many unresolved issues (e.g., magnetic curvature force, the optical corrugation, etc.).

There have been ongoing efforts to determine the magnetic field strength, inclination, and temperature of LBs. Typically, the optical depth is converted to a geometric scale, assuming hydrostatic equilibrium with the magnetic pressure term

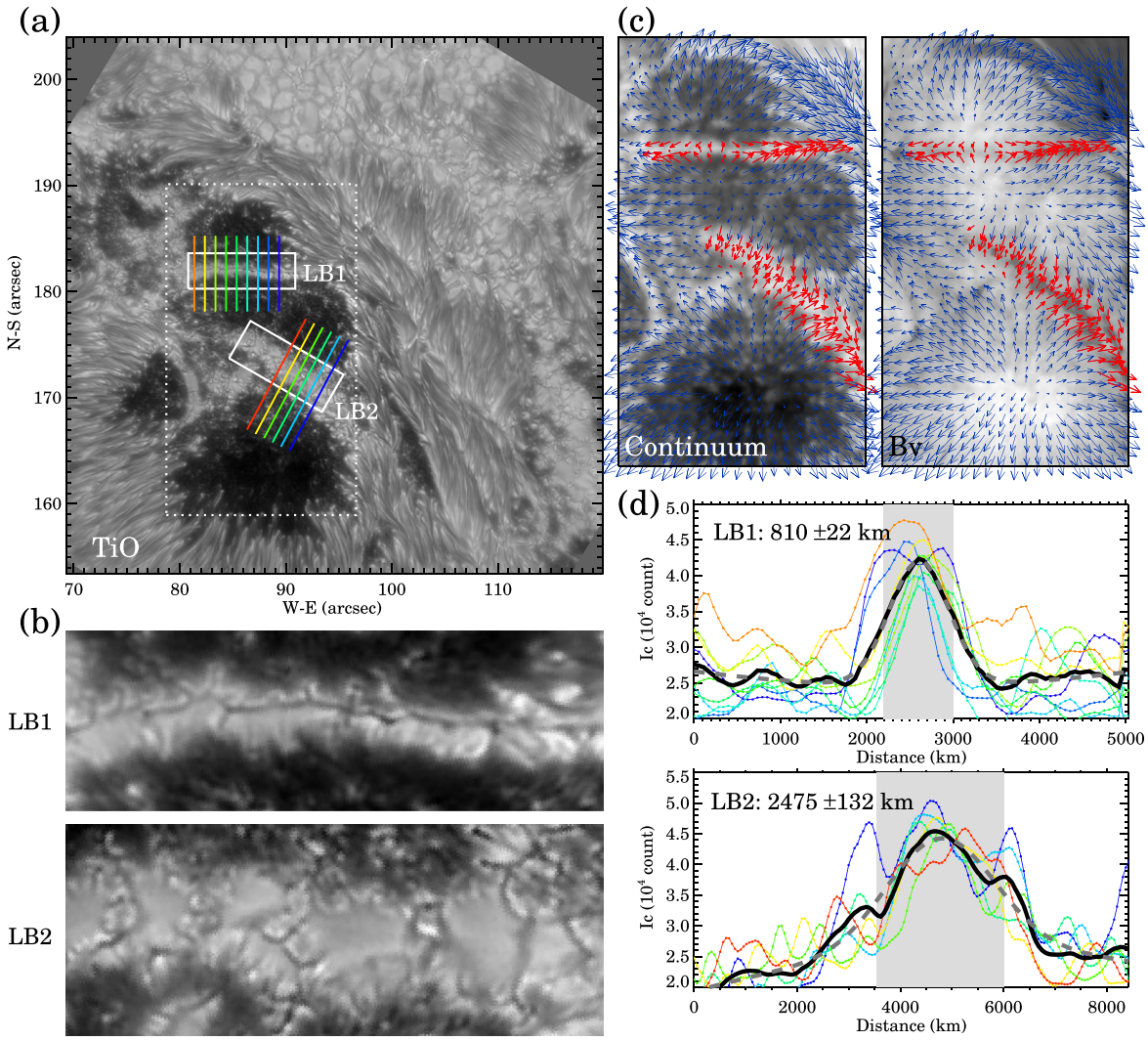

Figure 1. (a) A GST TiO snapshot of AR 12371 that shows the sunspot group and two LBs of interest (labeled LB1 and LB2, respectively). The two solid rectangle boxes are defined for the zoom-in TiO images of the two LBs shown in (b), and the slits crosscutting LB1 and LB2 show where the cross-sectional continuum intensities were measured. The large dotted rectangle box is drawn to mark the region of interest for the GST continuum and $\boldsymbol{B}_z$ images shown in (c). (b) The zoomed-in TiO images of LB1 and LB2. (c) GST continuum and $\boldsymbol{B}_z$ images, superimposed with arrows representing horizontal magnetic field vectors. The arrows in the two LBs are highlighted in red. (d) GST continuum intensity (I_c) profiles (with different colors) along the slits in (a), the mean intensity profile (black curve), and the Gaussian fit (gray dashed curve). For reference, the color of each profile is the same as the color of the slit (see panel (a)). The Gaussian FWHM and $\pm 3\sigma$ of LB1 and LB2 are provided.

included, taking into account the Wilson depression (Felipe et al. 2016). A new inversion code called FIRTEZ-dz (Pastor Yabar et al. 2019) can retrieve the magnetic field directly on the geometric scale, depending on the accuracy of the gas pressure or density. The incorporation of the magnetic curvature force in the FIRTEZ-dz code under the magnetohydrostatic equilibrium (Borrero et al. 2019) allows a more realistic determination of gas pressure, density, and other physical parameters (Borrero et al. 2021; Pastor Yabar et al. 2021). A table summarizing the existing results for the magnetic field strength, inclination, and temperature of LBs is available in Griñón-Marín et al. (2021). Although there are variations in the derived parameters depending on the adopted spectral lines and selected local regions, the distinction between LBs and umbrae is now unquestionable.

In this study, we used nonlinear force-free field (NLFFF) models extrapolated from the photospheric vector magnetograms to study the 3D magnetic structure of LBs. There are both advantages and disadvantages to this approach compared to the Stokes inversion method. The aforementioned inversion techniques for the stratified atmospheric structure can retrieve the fine-scale magnetic structure of LBs in the lower atmosphere insofar as the spectral lines offer opacity. On the other hand, with the NLFFF extrapolation, we can obtain parameters of the magnetic field over much larger height ranges. The resulting magnetic field vectors specified in a large 3D volume can be used to derive other magnetic parameters, such as magnetic shear, twist, and current density. The NLFFF model is, however, subject to the force-free assumption and does not provide plasma temperature and density information. The NLFFF model can thus provide a validation and complement to the spectral line inversion method in studying the 3D magnetic field structure of LBs.

2. GST Data

GST is a 1.6 m off-axis ground-based solar telescope at Big Bear Solar Observatory. Equipped with a high-order adaptive

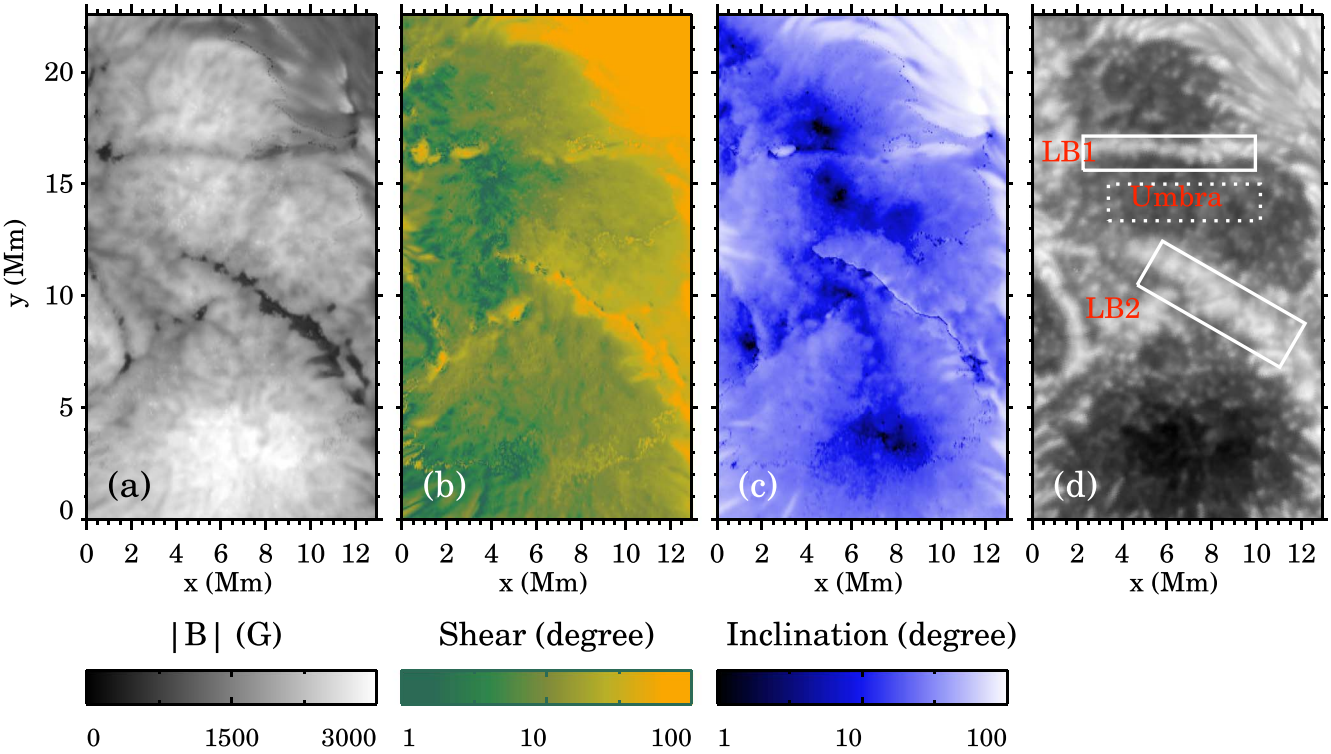

Figure 2. Spatial distribution of magnetic field strength (panel (a)), magnetic shear (panel (b)), inclination (panel (c)), and a continuum image (panel (d)). Boxes labeled LB1, LB2, and Umbra in panel (d) indicate the three regions, whose histograms are shown in Figure 3.

optics system and aided by the ex post facto speckle image reconstruction techniques, GST provides exceptionally high-resolution observations of the Sun. In this study, we mainly employ the following kinds of GST data: TiO (7057 Å, 10 Å bandpass, which is a good proxy of the visible continuum) images of the active region (AR) 12371, to observe the morphology and determine the position and size of LBs, and spectropolarimetric data (at Fe I 1565 nm doublet, 0.2 Å bandpass) to quantitatively measure the magnetic parameters and to extrapolate the NLFFF models as the bottom boundary conditions.

Specifically, TiO images, with a pixel scale of $\sim 0\farcs 04$, were taken by the Broad-band Filter Imager of GST. The spectropolarimetric data were obtained with the Near InfraRed Imaging Spectropolarimeter (NIRIS; Cao et al. 2012) of GST, equipped with the new infrared detector and the improved dual Fabry–Perot interferometer systems. The spectropolarimetric data were processed with the NIRIS data processing pipeline (Ahn et al. 2016), including dark and flat field correction, the calibration of instrumental crosstalk, and the Milne–Eddington Stokes inversion, from which key physical parameters, such as magnetic field strength, magnetic field inclination and azimuth, and Doppler velocity, could be extracted. These images and continuum images are with a pixel scale of $\sim 0\farcs 08$. Then, the intrinsic 180° azimuth ambiguity was resolved using ME0 code (Leka et al. 2009a, 2009b) based on the "minimum energy" algorithm (Metcalf 1994; Metcalf et al. 2006), and the projection effects were corrected by transforming the ambiguity-resolved magnetic field to heliographic coordinates (Gary & Hagyard 1990). We used only a set of vector magnetograms, a Dopplergram, and a continuum image, all taken at about 17:24 UT (before the initiation of an M6.5 flare in this AR), for the NLFFF extrapolation.

3. Analysis and Results

3.1. At the Photosphere

Figure 1(a) presents a GST TiO snapshot of the sunspot group taken on 2015 June 22 at ~17:24 UT in AR 12371. The two LBs of interest, labeled LB 1 and LB 2, and their host sunspots were close to the disk center. To better show the two LBs observed with high-resolution TiO, the solid rectangular boxes corresponding to the two LB regions in Figure 1(a) are shown enlarged in Figure 1(b). The narrow LB1 reveals a long central dark lane, intersected with short intergranular lanes or dark knots, running through the long axis of LB1. Such long and short lanes are regarded as manifestations of convective upflows and downflows, respectively (see, e.g., Zhang et al. 2018). The wider LB2, on the other hand, does not have a central dark lane, but exhibits a discernible photospheric granulation pattern. Figure 1(c) shows the NIRIS photospheric horizontal magnetic field vectors ($\boldsymbol{B}_x$, $\boldsymbol{B}_y$) superimposed on the continuum and $\boldsymbol{B}_z$ images, with the portion on the two LBs highlighted in red. Here ($\boldsymbol{B}_x$, $\boldsymbol{B}_y$, $\boldsymbol{B}_z$) refer to the heliographic (x, y, z) components of the magnetic field (Gary & Hagyard 1990), respectively, where the x-axis points to the solar west, the y-axis to the solar north, and the z-axis to the observer. Both LBs are sandwiched between the sunspot umbra of the same magnetic polarity (positive), and the magnetic field vectors fanning out from the neighboring umbra converge at LBs. We see that the azimuth aligns more with the long axis of the LBs near the ends of the LBs. Figure 1(d) shows the continuum intensity profiles of the two LBs along the colored slits in Figure 1(a) and the average of these curves (black curve) as well as its Gaussian fit curve (gray dashed curve). LB2 is considerably wider than LB1. The Gaussian FWHMs of LB1 and LB2 are 810 km and 2475 km, respectively.

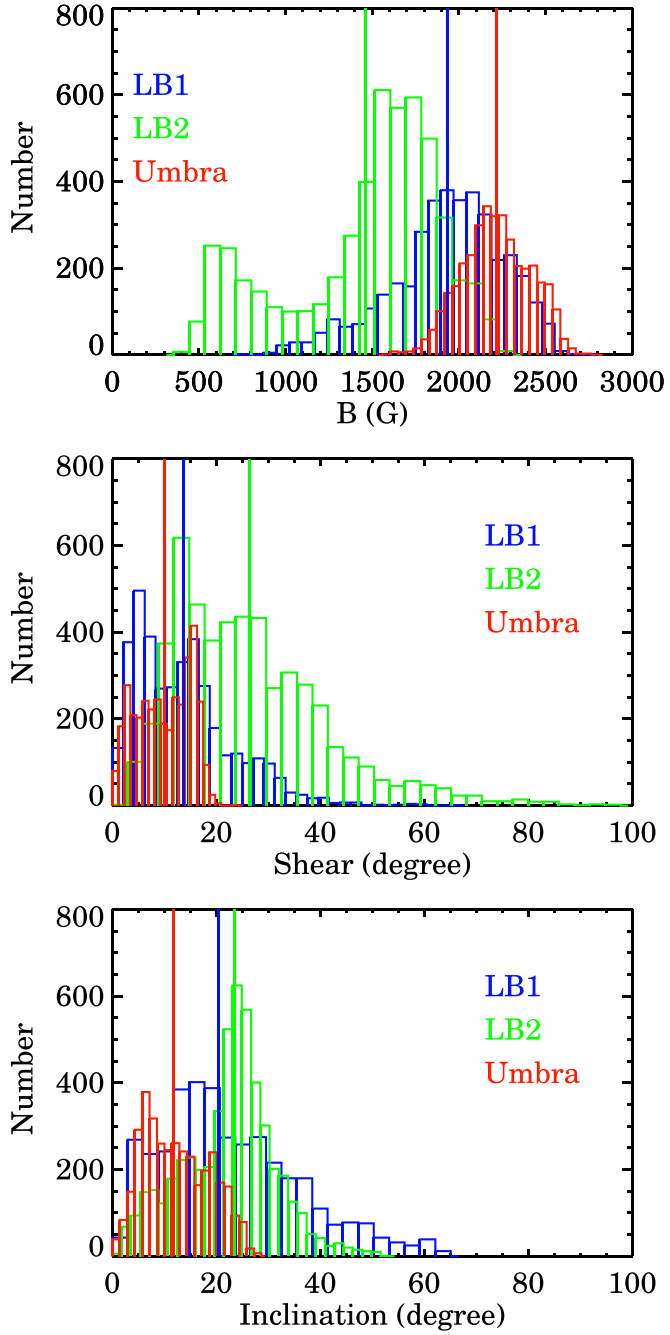

Figure 3. Histograms of magnetic field strength (top), shear (middle), and inclination (bottom) at the three regions (LB1, LB2, and the umbra, shown in Figure 2). The vertical lines indicate the mean values of each distribution.

In Figure 2, panels (a)–(c) show the maps of the following magnetic parameters, respectively: (a) magnetic field strength $|\boldsymbol{B}|$, calculated by $\sqrt{\boldsymbol{B}_x^2 + \boldsymbol{B}_y^2 + \boldsymbol{B}_z^2}$, (b) magnetic shear, i.e., the angle between the magnetic field vector $\boldsymbol{B}$ and the local potential field vector $\boldsymbol{B}_p$, calculated by $\cos^{-1}[\boldsymbol{B} \cdot \boldsymbol{B}_p/|\boldsymbol{B}||\boldsymbol{B}_p|]$, and (c) magnetic inclination, i.e., the angle between the observed magnetic field vector and the local vertical direction, calculated by $\tan^{-1}\boldsymbol{B}_h/\boldsymbol{B}_z$. To better show the positions of the two LBs, a continuum image is displayed in panel (d). Compared to the umbra, the magnetic fields on the two LBs are weaker, more sheared, and more horizontally oriented. The histograms of these parameters at the two LBs and one umbra region are shown in Figure 3. The difference between the umbra and the LBs is particularly evident for the wider LB2, whose average magnetic field strength is ∼750 G weaker than that of the umbra, whose average shear is ∼6° more than that of the umbra, and whose average inclination is ∼12° more than that of the umbra.

As mentioned in Section 1, the magnetic field strength and inclination of LBs obtained from previous studies have been summarized in Griñón-Marín et al. (2021). Our results are particularly similar to the latest study by Griñón-Marín et al. (2021), which used the same Fe I 1565 nm spectral line as NIRIS and the spatial resolution of the data is relatively similar to that of NIRIS. Specifically, in Griñón-Marín et al. (2021), the mean $|\boldsymbol{B}|$ of the LBs and umbra are 1800–2300 G and 2500 G, respectively, and the mean inclinations of LBs and umbra are 25°–30° and 17°, respectively. By comparison, in our study, these corresponding values are 1500–1900 G and 2200 G, and 20°–24° and 12°, respectively.

3.2. At the Solar Atmosphere

We investigate the 3D magnetic characteristics of LBs using the NLFFF extrapolation. Specifically, we extrapolate two NLFFF models (Model 1 and Model 2) from the photospheric vector magnetograms of 17:36 UT using the weighted optimization method (Wiegelmann 2004). From the NLFFF extrapolation result, we derive the magnetic topology and other magnetic parameters, such as magnetic shear, twist, and current density.

Model 1 is extrapolated from the full-resolution NIRIS magnetograms to show the magnetic structure at fine scales. Since the field of view (FOV) of the NIRIS magnetogram is small (shown as the square area surrounded by the white box in Figure 4(a)) and positive and negative fluxes are not well balanced, which may have an impact on the extrapolation results, Model 2 is extrapolated from the expanded FOV (shown as the entire FOV of Figure 4(a)) from lower-resolution Helioseismic and Magnetic Imager (HMI) magnetograms, with the NIRIS magnetograms of reduced resolution embedded in the middle. Model 2 serves to demonstrate the large-scale magnetic topology and to examine the impacts of a small FOV and unbalanced flux on Model 1. Since HMI and NIRIS use different spectral lines, Fe I 617.3 nm and Fe I 1565 nm, respectively, they do not sample the magnetic field exactly at the same height. However, the height difference is expected to be less than 70 km (Cabrera Solana et al. 2005), which is smaller than the grid size of Model 2 and also the thickness of the photosphere. We have therefore used the merged two different magnetograms (NIRIS embedded HMI) as the bottom boundary of the model and ignored the height offset between them.

Table 1 lists the properties and the domain-averaged extrapolation metrics, CW $\sin\theta$ and $|\nabla \cdot \boldsymbol{B}|$, of the two models, along with that of a potential field model extrapolated from the same boundary conditions as that of Model 2. Both the NLFFF models show very similar metrics, which are typical for the weighted optimization algorithm and suggest a moderately satisfied force-free and divergence-free condition. The overall magnetic topology obtained from the NLFFF Model 2 (Figure 4(c)) offers a truthful reconstruction of observations in comparison with the Atmospheric Imaging Assembly (AIA) 94 Å image (Figure 4(d)). We then compared the magnetic field vectors $\boldsymbol{B}_x$, $\boldsymbol{B}_y$, and $\boldsymbol{B}_z$ "voxel-by-voxel" on the same volume as Model 1. Since the two NLFFF models have different spatial

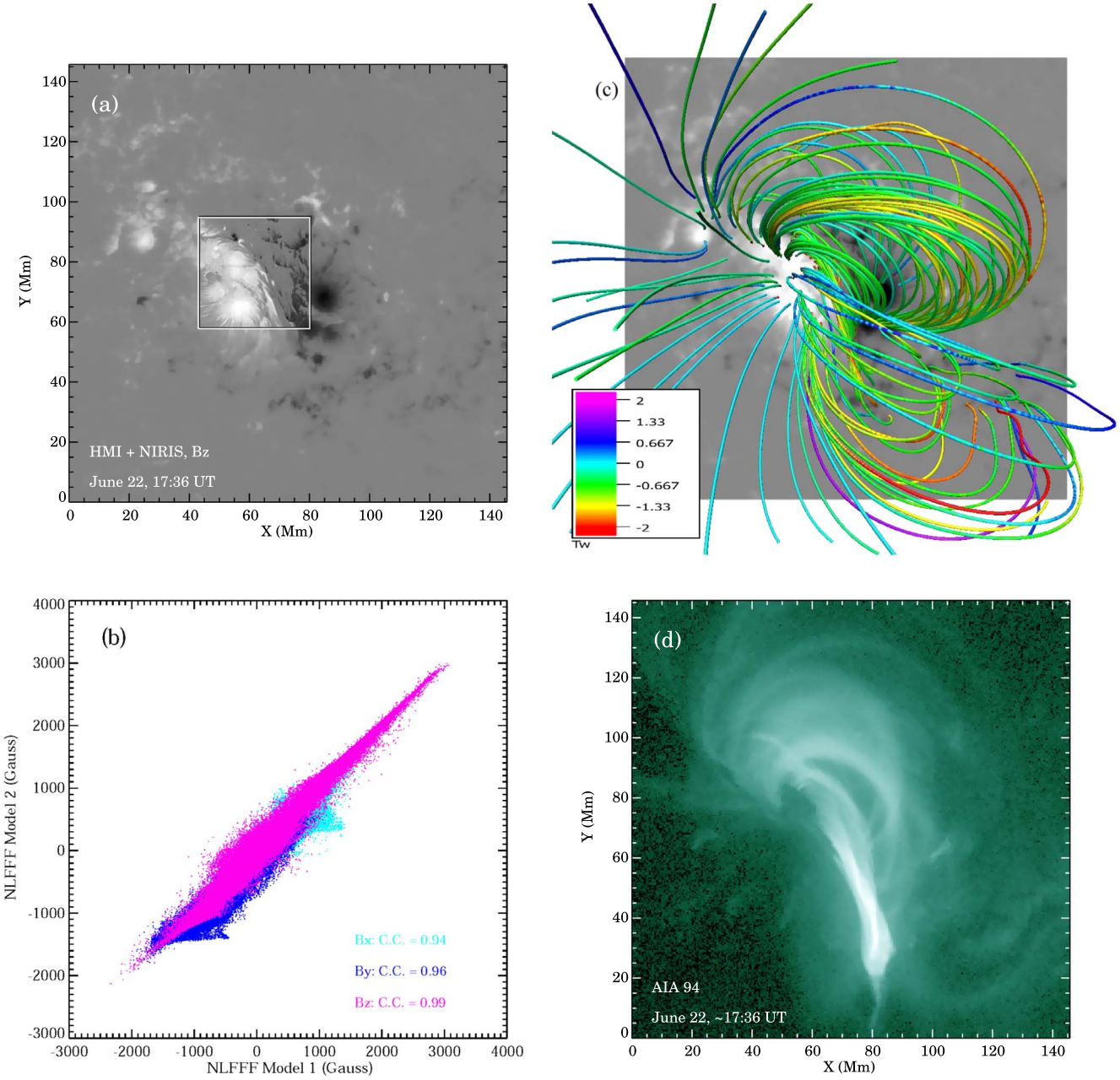

Figure 4. (a) The large field-of-view (FOV) HMI magnetogram $\boldsymbol{B}_z$ (∼145 Mm × 145 Mm) at 17:36 UT, 2015 June 22, with the small FOV NIRIS B_z (∼37 Mm × 37 Mm) of the same time embedded in the middle (enclosed by the square box). The small and large FOVs define the bottom boundaries of the NLFFF Models 1 and 2, respectively. (b) Scatterplots of the NLFFF Model 1 vs. the NLFFF Model 2 in the same volume as the NLFFF Model 1, in three components $\boldsymbol{B}_x$ (cyan), $\boldsymbol{B}_y$ (navy), and $\boldsymbol{B}_z$ (pink). The linear Pearson correlation coefficients are shown in the panel. (c) Magnetic field lines randomly selected from the NLFFF Model 2, with the color indicating the twist number T_w. (d) An EUV 94 Å image taken by SDO/AIA at 17:36 UT.

Table 1
Properties and Extrapolation Metrics of Models

Models	Pixel Scale	Dimensions	CW $\sin\theta$ [a]	$\lvert\nabla\cdot\boldsymbol{B}\rvert$
NLFFF Model 1	0.057 Mm	648 × 648 × 160 uniform grid points (∼37 × 37 × 9 Mm^3)	0.26	8.2×10^{-11} (G cm^{-1})
NLFFF Model 2	0.28 Mm	512 × 512 × 512 uniform grid points (∼145 × 145 × 145 Mm^3)	0.24	4.9×10^{-11} (G cm^{-1})
Potential model	0.28 Mm	512 × 512 × 512 uniform grid points (∼145 × 145 × 145 Mm^3)	N/A	3.6×10^{-12} (G cm^{-1})

Note.
[a] The current weighted average of $\sin\theta$ (Wheatland et al. 2000), where θ is the angle between the current density $\boldsymbol{J}$ and $\boldsymbol{B}$.

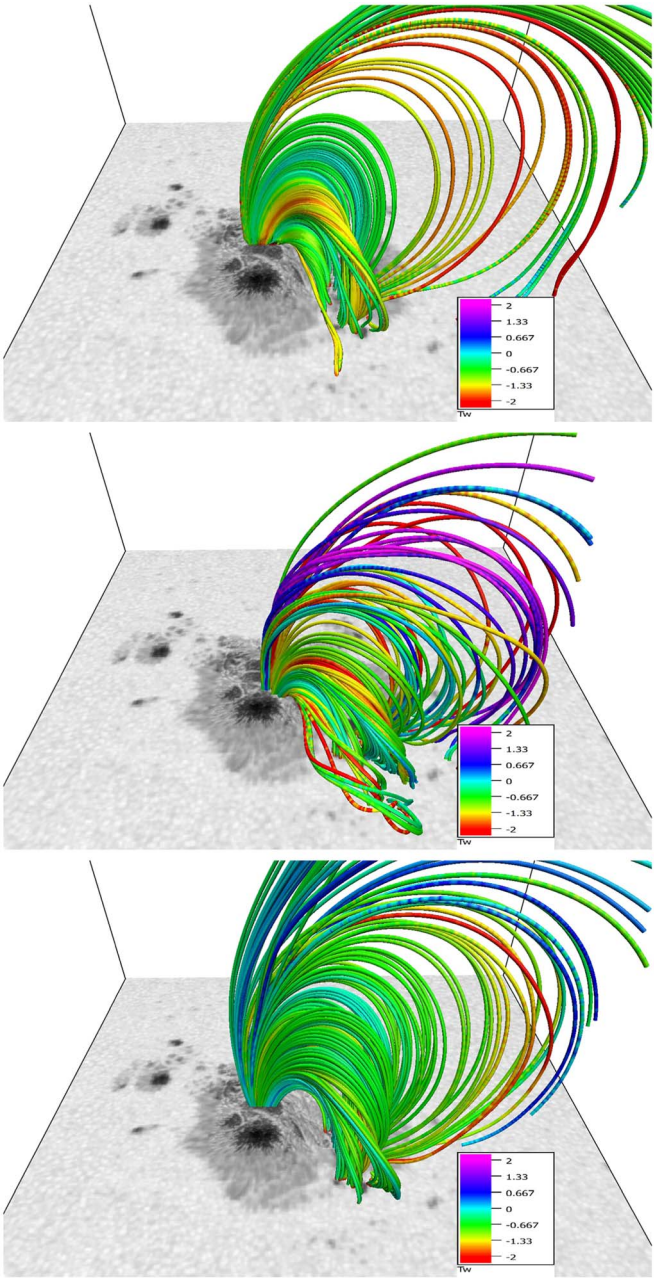

Figure 5. Magnetic field lines obtained from the NLFFF Model 2, with field lines originating from the locations of LB1 (top), LB2 (middle), and the umbra between LB1 and LB2 (bottom), respectively, superimposed over the continuum image. The color of the field lines indicates the value of the twist number T_w.

resolutions, we reduced the resolution of Model 1 to make it the same as that of Model 2 for such a "voxel-by-voxel" comparison. A very strong correlation between the two models is found (Figure 4(b)), indicating that the small FOV and the unbalanced flux of Model 1 do not have a serious impact on the extrapolation in this case. Therefore, we are confident in using the NLFFF Model 1 to characterize the fine-scale 3D magnetic structures.

Before showing the fine-scale magnetic structures, we use the NLFFF Model 2, which has a large FOV but at a lower resolution, to display the large-scale configuration of magnetic field lines emanating from the two LBs and the umbra in between, as shown in Figure 5. The color of the field lines indicates the value of the twist number ($T_w = \frac{1}{4\pi}\int_L \alpha dl$; Liu et al. 2016). Although not on a fine scale, this figure gives us an overall impression of the LB magnetic fields. Apparently, the magnetic field lines from the two LBs exhibit a stronger nonpotentiality, shown in a greater degree of twist and complexity, than the magnetic lines from the umbra.

We use the NLFFF Model 1, which has a high spatial resolution and a small FOV to show the fine-scale magnetic structures in Figures 6–10. Figures 6 and 7 show the stratification of the same magnetic parameters of LB1 and LB2 as analyzed in Figures 2 and 3 at geometrical heights. The curves at each height layer represent the average of magnetic parameters at multiple slits at this layer. At the low layers near the surface, the magnetic fields on LBs show a lower field strength, a larger inclination angle, and a larger shear angle compared to the umbrae, as noted before. As height increases, such differences become less and less conspicuous until a certain height where the gap disappears. It is worth noting that the field strength at the non-bridge umbral regions decreases monotonically with height, while the magnetic field strength at the center of the LBs (especially the wider LB2) increases with height in a certain range close to the surface. Specifically, the field strength at the center of LB2 is ~800 G at $z = 0$ km and increases to ~1400 G at $z = 1000$ km, and then decreases with height. The narrower LB1 shows a much higher field strength at $z = 0$ km, 1800 G, and a much lower range of variation (about 100 G increase over a range of 400 km), but exhibits the same trend. Correspondingly, the inclination of both LBs decreases sharply compared to the neighboring umbrae, especially LB2, which decreases by at least 10° over a height range of 600 km. This implies that the magnetic lines above the LBs shift to a more vertical direction in the low atmosphere layers. Such changes in field strength and inclination are in accordance with the expected behavior of a low-lying magnetic canopy structure above LBs. At the same time, not surprisingly, as shown in Figure 1(c), we see an increased shear at the two LBs, and this shear decreases with height.

Figure 8 also demonstrates the inclination variation with height over LB1, LB2, and the umbral region between them for comparisons. Near the surface, the inclination angles of the two LBs are more widely distributed, 0°–5°, indicating the presence of more horizontal field vectors over the LB region, while, in contrast, the inclination angles in the umbrae regions are distributed in a relatively concentrated range, 0°–30°, which is in agreement with the results by Griñón-Marín et al. (2021). As the height increases, the inclination of the magnetic field over the LBs changes significantly to a more vertical direction. This change is particularly noticeable on LB2, with a reduction of ~15° of mean inclination angle over a height range of 1000 km. In contrast to the two LBs, the distributions of inclination over the umbra region remain essentially the same, with much less pronounced variation with height. This variation of inclination with height again coincides well with the expected behavior of the canopy structure above the LBs.

We compare our results obtained from the NLFFF model with previous results obtained from the Stokes inversion methods summarized in Griñón-Marín et al. (2021). There are, in fact, not many results for LBs over multilayers available for comparison, and those from Jurčák et al. (2006) are among the few that can directly be compared with those of the NLFFF model. Jurčák et al. (2006) show that from the solar surface to a height of 200 km, the magnetic field strength of LBs increases by ~400–700 G; in the same height range, the inclination of the

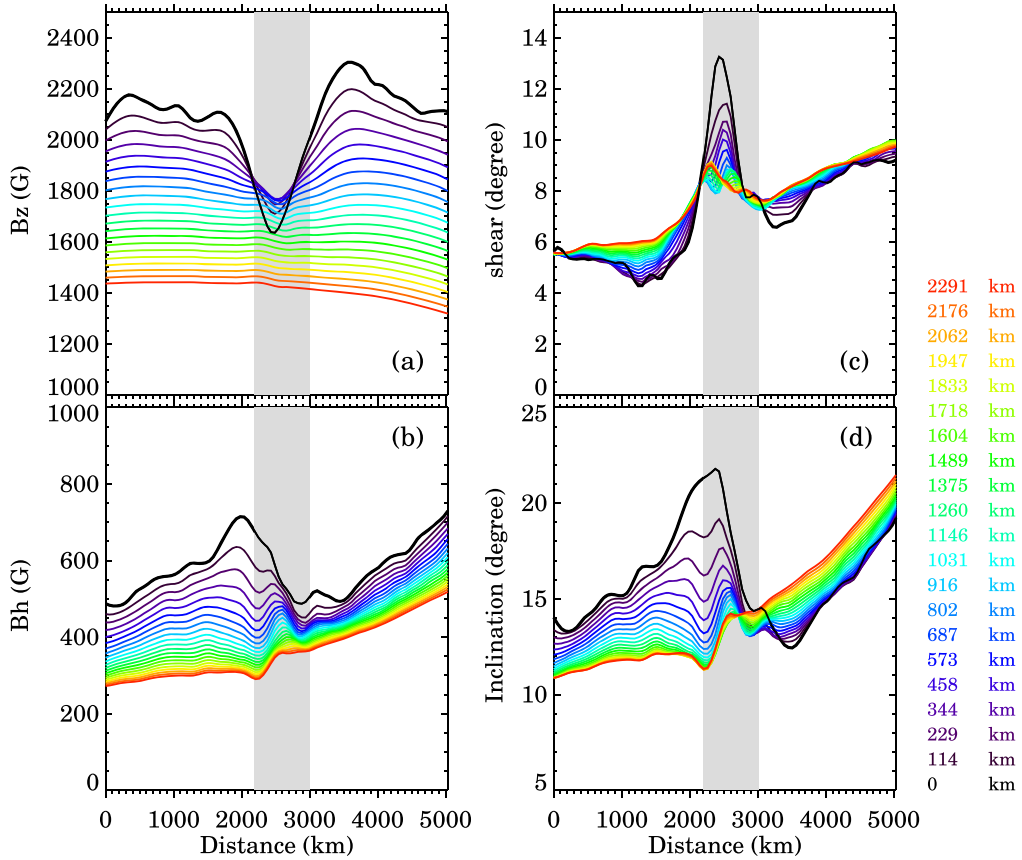

Figure 6. The stratification of magnetic parameters of LB1 at different layers: vertical and horizontal components of the magnetic field (panels (a) and (b), respectively), magnetic shear (panel (c)), and inclination (panel (d)). The curves at each layer represent the average of these magnetic parameters at multiple slit positions in this layer of the NLFFF Model 1. The height information of the averaged profiles is given on the right, corresponding by color. The shaded region in each panel indicates the approximate position of the LB1, estimated from the Gaussian FWHM of the continuum intensity.

LBs decreases by about 4°–7°. These results are similar to our results obtained from the NLFFF model. In addition, the NLFFF model shows that the magnetic field of LBs can increase with height in a range up to ∼1000 km, which is beyond the range that can be diagnosed by the Stokes inversion methods.

Figure 9 shows vertical slices of the magnetic field strength $|\boldsymbol{B}|$, electric current density $|\boldsymbol{J}| = |\nabla \times \boldsymbol{B}|/\mu_0$, and inclination angle, obtained from the NLFFF Model 1. $|\boldsymbol{B}|$ and inclination angle are two important characteristics to distinguish LBs from nearby umbra, and current density $\boldsymbol{J}$ is also important because it provides a quantitative measure of the deviation from a potential configuration, indicating an increase in stored magnetic energy (Leka 1997). The positions of the two cuts through LB1 and LB2 are indicated by the lines in Figure 8(a). Apparently, there is a weak-field character inside these two LBs, above which magnetic field lines away from the two umbrae converge to a more vertical direction, and hence form a cusp-like configuration. The height of this cusp is about 500 km, which can be better seen in the superimposed vectors in the $|\boldsymbol{B}|$ slice and in the low-lying, more horizontal region in the inclination slice. Such a configuration is particularly evident above LB2. It is also clear that strong electric currents above the LBs extend vertically from the surface up to 2500 km. At photospheric heights, $|\boldsymbol{J}|$ of the LBs averages about 0.2 A m^{-2} and can be as high as 0.6 A m^{-2}. At the low atmosphere, such as at a height of 740 km, the average $|\boldsymbol{J}|$ of the LBs decreases slightly ranging from 0.1 to 0.17 A m^{-2}. In contrast, the average $|\boldsymbol{J}|$ of the nearby umbra is 1 order of magnitude less than that of the LBs. In previous studies of LBs, the typical values of the z-component of current density $|\boldsymbol{J}_z|$ alone at photospheric heights range from 0.04 to 0.1 A m^{-2} (Leka 1997), reaching a maximum value of 0.2 A m^{-2} (Jurčák et al. 2006). The actual current density $|\boldsymbol{J}|$ is expected to be larger than the values of $|\boldsymbol{J}_z|$. In a non-force-free magnetic field model above an LB, the LB is also a site of strong $|\boldsymbol{J}|$, which is ∼0.3 A m^{-2} at the photosphere and decreases monotonically to 0.06 A m^{-2} at a height of 900 km (Louis et al. 2021). Our results are comparable to those found previously, but certainly at the high end.

Figure 10 shows the spatial distribution of electric current density over the entire volume of the NLFFF Model 1. The strong electric currents are mainly concentrated around the magnetic polarity inversion line on the right side of the sunspot group, indicating that a large amount of magnetic free energy is stored there. We also found enhanced electric currents in the LB region as well as in some of the penumbral regions. In particular, the electric currents distributed throughout the LB2 form a current sheet extending vertically. The presence of such a vertical current sheet indicates that the magnetic field connectivity changes rapidly in the LB areas. As a comparison, the umbrae have negligible currents overall.

3.3. Doppler Velocity in LBs

GST data can provide not only magnetic field but Doppler velocity. The accuracy of the Doppler velocity depends on the quality of the fit to the Stokes profiles and also a number of

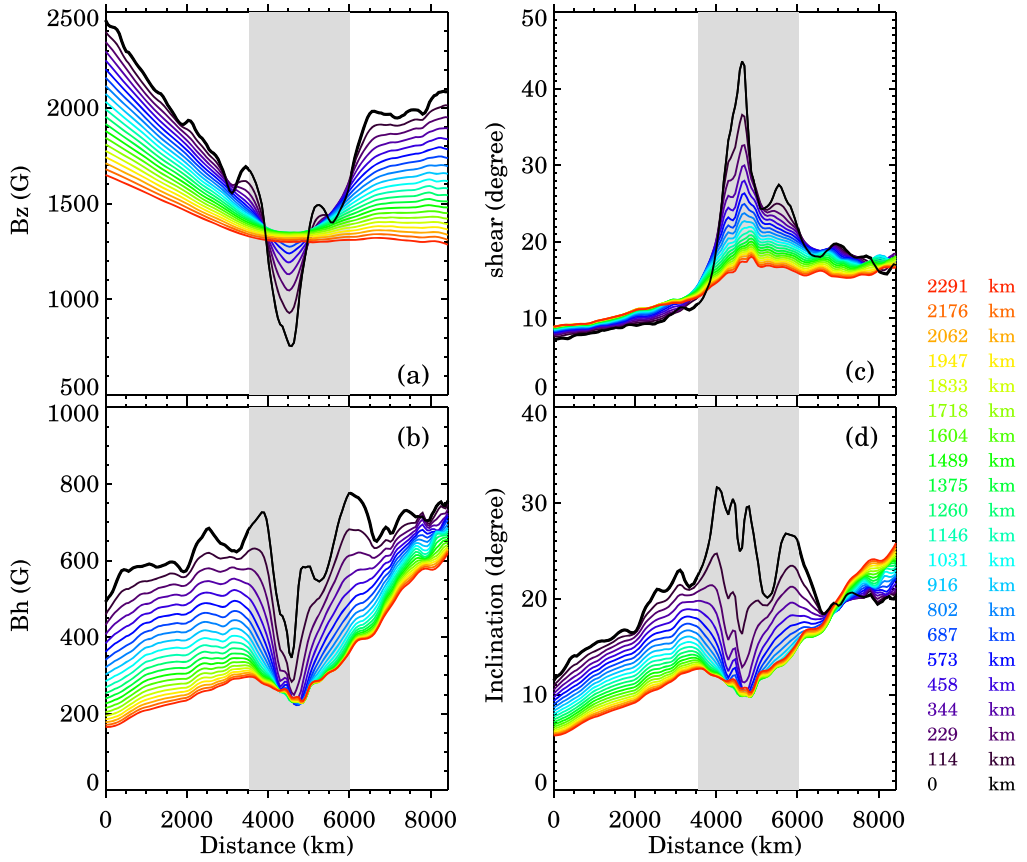

Figure 7. Same as for Figure 6, but for LB2.

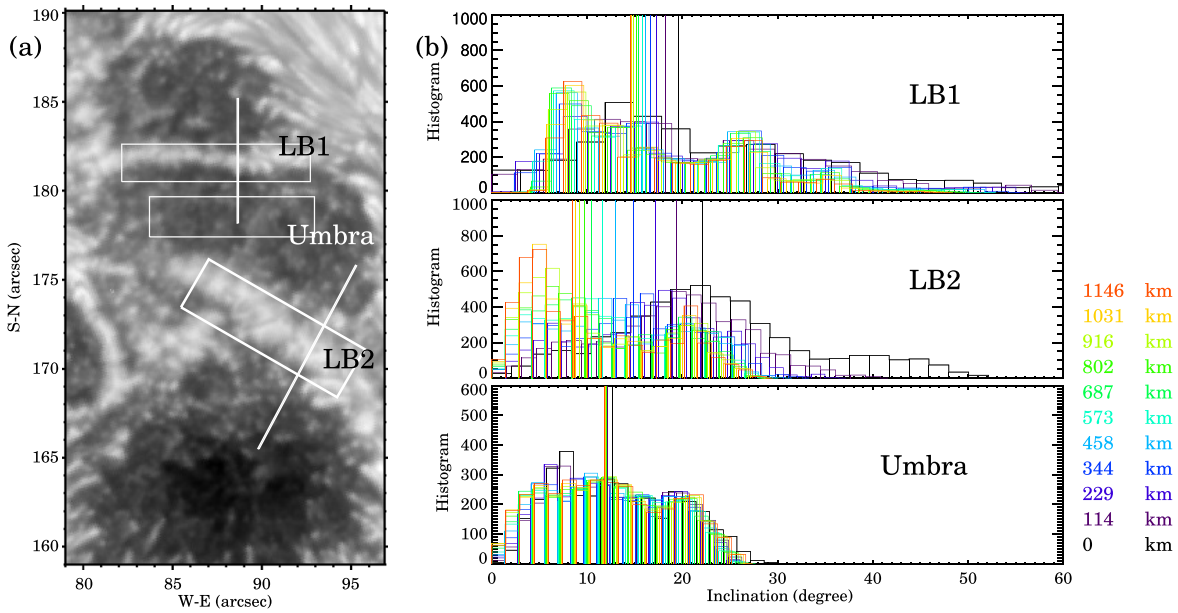

Figure 8. (a) The continuum image of the LBs and umbrae. Boxes labeled LB1, LB2, and Umbra show the three regions analyzed in (b). The two slits across LB1 and LB2 indicate the locations of the vertical cuts shown in Figure 9. (b) Histograms of inclination at different heights above the three regions (LB1, LB2, and the umbra), obtained from the NLFFF Model 1. The vertical lines indicate the median of each distribution.

issues, including the line asymmetry, data noise, and zero-point drift. To calibrate the Dopplergram, we set the average Doppler velocity of quiescent regions (outside the sunspots and with clearly visible granular patterns) to zero. We also checked the Doppler velocities obtained by NIRIS against those obtained by Hinode in the same AR at close times.

As shown in Figure 1, LB2 shows a discernible granular pattern, while the width of the narrow LB1 is barely a granule size, and only a central dark lane along the LB axis is seen. This central dark lane is presumably the result of a locally elevated optical depth $\tau = 1$ surface formed by the piling up of convective plasma in the center (Rouppe van der Voort et al. 2010). In

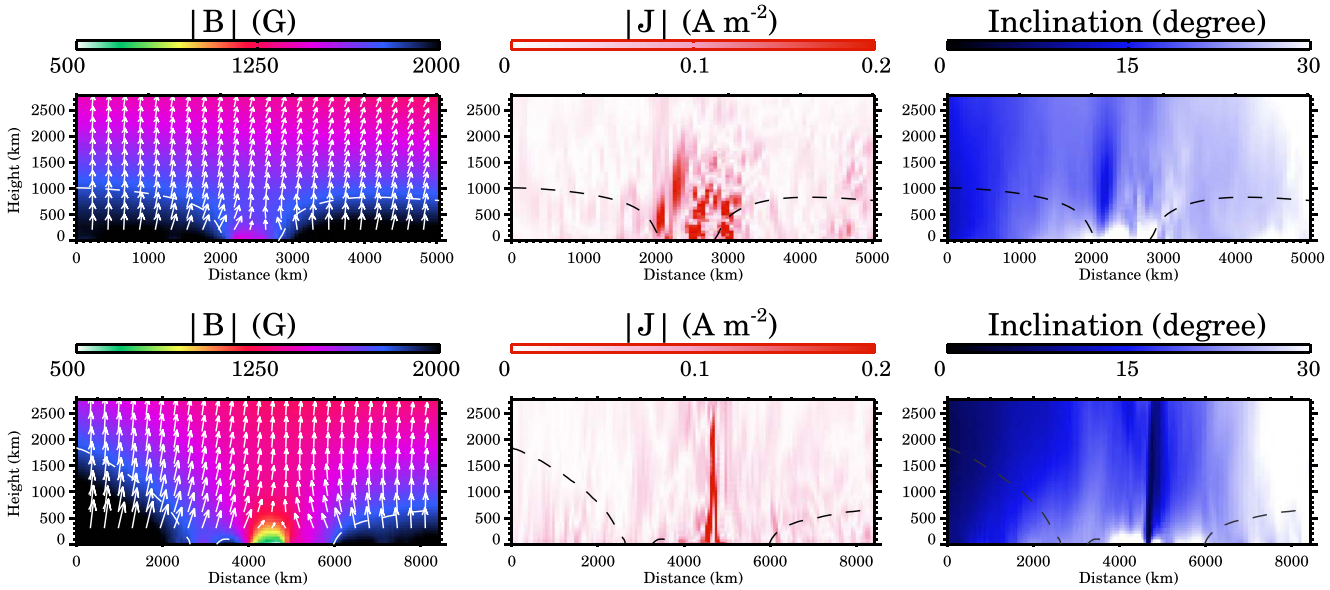

Figure 9. Vertical cross-sectional slices through the two slits of LB1 and LB2 (see Figure 8(a)) that were obtained from the NLFFF Model 1. Panels show, from left to right, the magnetic field strength superimposed with the projection of magnetic field vectors onto the plane, the electric current density, and the magnetic field inclination. A 1800 G contour line (white dashed curves) is overplotted to outline the strong magnetic field region (black).

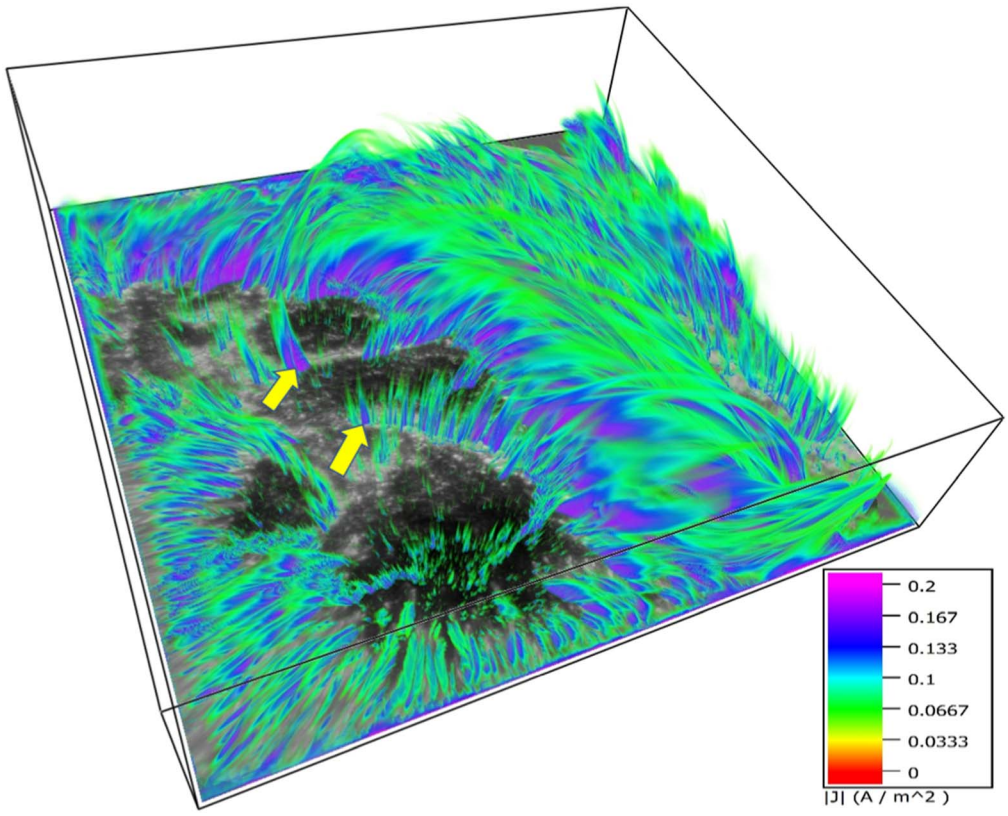

Figure 10. Spatial distribution of electric current density over the volume of the NLFFF Model 1. The arrows mark some enhanced currents above the LBs. The size of this computing box is 648 × 648 × 160 grid points (∼37 × 37 × 9 Mm^3) as listed in Table 1.

contrast to intergranular lanes located at the sides of a convection cell, which are associated with downflows, the central dark lane usually corresponds to upflows, as hinted by some MHD simulations of umbral dots (Schüssler & Vögler 2006) or penumbral filaments (Heinemann 2007; Nordlund 2010), which also have a central dark lane reminiscent of the dark lane observed in LBs. The upflows at the central dark lane of LBs and the convective nature of the LB granules are later confirmed in several high-resolution observations (Rouppe van der Voort et al. 2010; Lagg et al. 2014; Zhang et al. 2018).

Here we also try to investigate the Doppler velocity pattern of the two LBs using NIRIS Dopplergrams. Figure 11 shows the zoomed-in TiO images of LB1 and LB2 and their

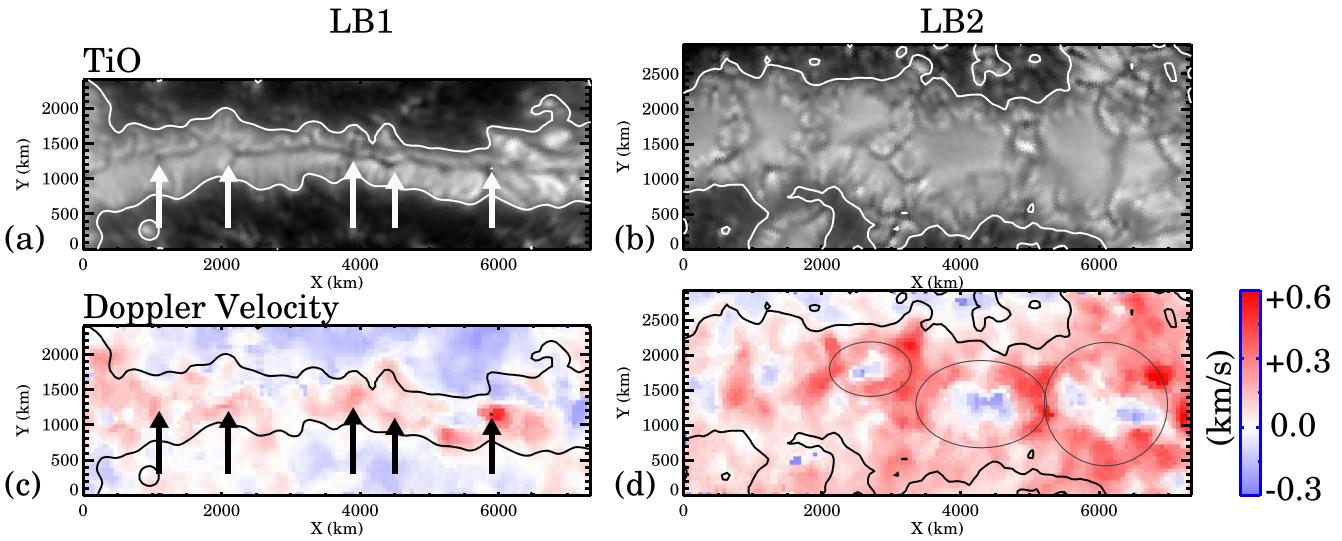

Figure 11. (a)–(b) TiO images of LB1 and LB2, which are the same as Figure 1(b). (c)–(d) Dopplergrams of LB1 and LB2, with positive values (red color) representing downflows and negative values (blue color) representing upflows. The white/black contours in the TiO and Dopplergram images delineate the edges of the two LBs. The arrows in (a) and (c) indicate the location of some dark knots in the TiO, which correspond to downflows in the Dopplergram. The ellipses in (d) mark some granular cells.

corresponding Dopplergrams, in which positive/negative values (red/blue colors) represent downflows/upflows. The Dopplergram of LB2 shows the same convective pattern as quiet-Sun granules, i.e., the central upflows are surrounded by downflows (marked by the ellipses), except that the downflow along the LB edge is fainter than that across the LB. Perhaps the strong umbral magnetic fields on both sides constrain the convective divergence, making it mainly along the LB direction. On the other hand, the Dopplergram of the narrow LB1 does not show a clear convective pattern. Instead, LB1 consists of intermittent patches of downflows and upflows. The downflow fragments are seemingly associated with dark knots in the central dark lane. As suggested by Zhang et al. (2018), these dark knots have the same origin as the intergranular lanes and therefore exhibit convective downflows.

4. Conclusions

In this paper, we studied two LBs: a narrow LB (with width ~810 km) and a considerably wider LB (2475 km) in the AR NOAA 12371 using the high-resolution vector magnetogram data from the GST/NIRIS and the NLFFF model extrapolated from both the photospheric magnetogram from GST/NIRIS and that from the Solar Dynamics Observatory (SDO)/HMI, which allow us to determine both the small- and large-scale magnetic structures. The high-resolution magnetogram data and the NLFFF model show the presence of a field-free, or more precisely, weak-field, region inside the LBs. The weak-field region is covered by the canopy of the stronger and more vertical magnetic field, and this canopy structure is filled with substantial electric currents extending up to the upper atmosphere. The canopy structure is more evident in LB2, which is wider and shows the granular pattern more clearly. The magnetic canopy structure obtained here with the NLFFF model is similar in both shape and quantitative magnetic field strength and inclination to previous results obtained from the radiative transfer inversion methods with depth stratification.

We found that the wide LB2 shows the same convective pattern as quiet-Sun granules. The downward velocity of LB2 averages 0.3 km s^{-1}, and reaches up to 0.8 km s^{-1}, while the upward velocity averages 0.1–0.2 km s^{-1}. Notably, a previous simulation has shown that LBs with discernible granular-looking patterns are more deeply rooted in the underlying convective zone, about 3–12 Mm below the solar surface (Rempel 2011). The strong downflow, which could be up to 10 km s^{-1}, is another sign of deep anchoring since granular downflows tend to accelerate with depth (Lagg et al. 2014). On the other hand, the narrow LBs or umbral dots can be the product of surface magnetoconvection and occur 1-2 Mm below the solar surface (Schüssler & Vögler 2006).

Our observations and analyses allow us to glimpse the canopy structure and obtain quantitative measurements of its shape, dimension, current density, and Doppler velocity. The results will be important for the study of magnetic reconnection and heating mechanisms in the chromosphere since this magnetic canopy around the LB is associated with various dynamic phenomena of chromospheric activity.

On large scales, we find a substantial difference between the LBs and umbrae in that the field lines emanating from the two LBs are more twisted than those from the neighboring umbrae (Figure 5). This difference may be related to the formation mechanism of LBs. A numerical MHD simulation shows that a buoyant magnetic flux bundle rises from a convective zone to the photospheric layer during the formation phase of an AR (Cheung et al. 2010). In another simulation by Toriumi et al. (2015a), magnetic field lines in the LB are highly twisted with a serpentine structure below the visible surface, and are being continuously transported to the surface by convective upflows. Although these magnetic field lines undergo unraveling due to reduced tension force as they rise into the corona, some of the twist may still be retained, as found in our NLFFF model. Future simulations can help to clarify the topology of the magnetic fields as they evolve.

Acknowledgments

We gratefully acknowledge the use of data from the Goode Solar Telescope (GST) of the Big Bear Solar Observatory (BBSO). BBSO operation is supported by US NSF AGS-2309939 and AGS-1821294 grants and New Jersey Institute of

Technology. GST operation is partly supported by the Korea Astronomy and Space Science Institute and the Seoul National University. We also thank the NASA SDO team for HMI and AIA data. HMI and AIA are instruments on board SDO, a mission for NASA's Living with a Star program. J.J., N.L., J.L., Y.X., W.C., and H.W. were supported by NASA grants 80NSSC23K0406 (HGI), 80NSSC21K1671 (HSR), 80NSSC21K0003 (LWS), 80NSSC20K0025, 80NSSC19K0068, 80NSSC19K0257, and 80NSSC19K0859, and NSF grants AST-2108235, AGS-1927578, 1954737, 2114201, 2149748, 2206424, 2300341, and 2309939.

ORCID iDs

Ju Jing https://orcid.org/0000-0002-8179-3625
Nian Liu https://orcid.org/0000-0002-6018-3799
Jeongwoo Lee https://orcid.org/0000-0002-5865-7924
Wenda Cao https://orcid.org/0000-0003-2427-6047
Haimin Wang https://orcid.org/0000-0002-5233-565X

References

Ahn, K., Cao, W., Shumko, S., & Chae, J. 2016, AAS/Solar Physics Division Meeting, 47, 2.07
Beckers, J. M., & Schröter, E. H. 1969, SoPh, 10, 384
Bharti, L. 2015, MNRAS, 452, L16
Borrero, J. M., Pastor Yabar, A., Rempel, M., & Ruiz Cobo, B. 2019, A&A, 632, A111
Borrero, J. M., Pastor Yabar, A., & Ruiz Cobo, B. 2021, A&A, 647, A190
Cabrera Solana, D., Bellot Rubio, L. R., & del Toro Iniesta, J. C. 2005, A&A, 439, 687
Cao, W., Goode, P. R., Ahn, K., et al. 2012, in ASP Conf. Ser. 463, Second ATST-EAST Meeting: Magnetic Fields from the Photosphere to the Corona, ed. T. R. Rimmele et al. (San Francisco, CA: ASP), 291
Cao, W., Gorceix, N., Coulter, R., et al. 2010, AN, 331, 636
Cheung, M. C. M., Rempel, M., Title, A. M., & Schüssler, M. 2010, ApJ, 720, 233
Choudhuri, A. R. 1986, ApJ, 302, 809
Felipe, T., Collados, M., Khomenko, E., et al. 2016, A&A, 596, A59
Gary, G. A., & Hagyard, M. J. 1990, SoPh, 126, 21
Goode, P. R., & Cao, W. 2012, in ASP Conf. Ser. 463, Second ATST-EAST Meeting: Magnetic Fields from the Photosphere to the Corona, ed. T. R. Rimmele et al. (San Francisco, CA: ASP), 357
Griñón-Marín, A. B., Pastor Yabar, A., Centeno, R., & Socas-Navarro, H. 2021, A&A, 647, A148
Heinemann, T., Nordlund, Å, Scharmer, G. B., & Spruit, H. C. 2007, ApJ, 669, 1390
Hirzberger, J., Bonet, J. A., Sobotka, M., Vázquez, M., & Hanslmeier, A. 2002, A&A, 383, 275
Jurčák, J., Martínez Pillet, V., & Sobotka, M. 2006, A&A, 453, 1079
Lagg, A., Solanki, S. K., van Noort, M., & Danilovic, S. 2014, A&A, 568, A60
Leka, K. D. 1997, ApJ, 484, 900
Leka, K. D., Barnes, G., & Crouch, A. 2009a, in ASP Conf. Ser. 415, The Second Hinode Science Meeting: Beyond Discovery-Toward Understanding, ed. B. Lites et al. (San Francisco, CA: ASP), 365
Leka, K. D., Barnes, G., Crouch, A. D., et al. 2009b, SoPh, 260, 83
Lim, E.-K., Yang, H., Yurchyshyn, V., et al. 2020, ApJ, 904, 84
Lites, B. W., Bida, T. A., Johannesson, A., & Scharmer, G. B. 1991, ApJ, 373, 683
Liu, R., Kliem, B., Titov, V. S., et al. 2016, ApJ, 818, 148
Louis, R. E., Bellot Rubio, L. R., de la Cruz Rodríguez, J., Socas-Navarro, H., & Ortiz, A. 2015, A&A, 584, A1
Louis, R. E., Prasad, A., Beck, C., Choudhary, D. P., & Yalim, M. S. 2021, A&A, 652, L4
Metcalf, T. R. 1994, SoPh, 155, 235
Metcalf, T. R., Leka, K. D., Barnes, G., et al. 2006, SoPh, 237, 267
Parker, E. N. 1979, ApJ, 234, 333
Pastor Yabar, A., Borrero, J. M., Quintero Noda, C., & Ruiz Cobo, B. 2021, A&A, 656, L20
Pastor Yabar, A., Borrero, J. M., & Ruiz Cobo, B. 2019, A&A, 629, A24
Rempel, M. 2011, ApJ, 729, 5
Rempel, M., Schüssler, M., & Knölker, M. 2009, ApJ, 691, 640
Robustini, C., Leenaarts, J., de la Cruz Rodriguez, J., & Rouppe van der Voort, L. 2016, A&A, 590, A57
Rouppe van der Voort, L., Bellot Rubio, L. R., & Ortiz, A. 2010, ApJL, 718, L78
Rueedi, I., Solanki, S. K., & Livingston, W. 1995, A&A, 302, 543
Ruiz Cobo, B., & del Toro Iniesta, J. C. 1992, ApJ, 398, 375
Nordlund, Å, & Scharmer, G. B. 2010, in Magnetic Coupling between the Interior and Atmosphere of the Sun, ed. S. S. Hasan & R. J. Rutten (Berlin: Springer), 243
Scharmer, G. B., Bjelksjo, K., Korhonen, T. K., Lindberg, B., & Petterson, B. 2003, Proc. SPIE, 4853, 341
Schüssler, M., & Vögler, A. 2006, ApJL, 641, L73
Shimizu, T. 2011, ApJ, 738, 83
Spruit, H. C., & Scharmer, G. B. 2006, A&A, 447, 343
Tian, H., Yurchyshyn, V., Peter, H., et al. 2018, ApJ, 854, 92
Toriumi, S., Cheung, M. C. M., & Katsukawa, Y. 2015a, ApJ, 811, 138
Toriumi, S., Katsukawa, Y., & Cheung, M. C. M. 2015b, ApJ, 811, 137
Wheatland, M. S., Sturrock, P. A., & Roumeliotis, G. 2000, ApJ, 540, 1150
Wiegelmann, T. 2004, SoPh, 219, 87
Yang, S., Zhang, J., & Erdélyi, R. 2016, ApJL, 833, L18
Zhang, J., Tian, H., Solanki, S. K., et al. 2018, ApJ, 865, 29